Coupled Systems Mechanics, *Vol. 4, No. 1 (2015) 1-18*
DOI: http://dx.doi.org/10.12989/csm.2015.4.1.001

Localized particle boundary condition enforcements for the state-based peridynamics

C.T. Wu*[1] and Bo Ren[2]

[1]*Livermore Software Technology Corporation, 7374 Las Positas Road, Livermore, CA 94551, USA*
[2]*Department of Civil and Environmental Engineering, University of California, Berkeley CA 94720, USA*

(Received November 24, 2014, Revised March 5, 2015, Accepted March 8, 2015)

Abstract. The state-based peridynamics is considered a nonlocal method in which the equations of motion utilize integral form as opposed to the partial differential equations in the classical continuum mechanics. As a result, the enforcement of boundary conditions in solid mechanics analyses cannot follow the standard way as in a classical continuum theory. In this paper, a new approach for the boundary condition enforcement in the state-based peridynamic formulation is presented. The new method is first formulated based on a convex kernel approximation to restore the Kronecker-delta property on the boundary in 1-D case. The convex kernel approximation is further localized near the boundary to meet the condition that recovers the correct boundary particle forces. The new formulation is extended to the two-dimensional problem and is shown to reserve the conservation of linear momentum and angular momentum. Three numerical benchmarks are provided to demonstrate the effectiveness and accuracy of the proposed approach.

Keywords: state-based; peridynamics; convex kernel approximation; boundary condition

1. Introduction

Modelling the material response subjected to environments and loads at multiple time and spatial scales is considered important for the next generation of materials modeling. In spite of great efforts in attempting to coarse-grain molecular dynamics (MD) or couple it to meso- and macro-scale models (Curtin and Miller 2003, Seleson and Gunzburger 2010), challenges (cf. e.g., de Pablo and Curtin 2007) remain at closing the gap between the range of validity of classical continuum model and the MD model. To bypass this difficulty as well as to overcome enormous computing power and length scales limitations in the multi-scale modelling, the developments of multi-resolution material models (McVeigh and Liu 2008, Belytschko *et al*. 2014), combined quasi-continuum and micro-continuum models (Parks *et al*. 2008, Zhang and Gunzburger 2010, Ren and Li 2013), weakly coupled multi-scale (Watanabe and Terada 2010) or single/mono-material models (Askari *et al*. 2008) become alternative attractive to the industrial community. The peridynamics (Silling 2000) is considered a type of single/mono-material models that provides the information about fine-scale kinematics for the multi-scale material failure analyses (see (Seleson *et al*. 2009, Chen and Gunzburger 2011) for a detailed introduction and

*Corresponding author, Dr., E-mail: ctwu@lstc.com

http://www.techno-press.org/?journal=csm&subpage=7 ISSN: 2234-2184 (Print), 2234-2192 (Online)

therein references).

Original peridynamic model, the so-called bond-based peridynamics (Silling 2000), was introduced to describe the formation of discontinuities. In contrast to the classical local and nonlocal theories (Chen *et al.* 2000, Bazant and Jirasek 2002), the peridynamic equation of motion is free of any spatial derivatives of displacement. The bond-based peridynamics assumes that each peridynamic bond responds independently of all the others, thus is restricted to a Poisson's ratio of 0.25 for isotropic linear elastic solids. To address this lack of generality, the state-based peridynamics (Siling *et al*. 2007) was introduced. The state-based peridynamics is a generalization of the bond-based peridynamic framework which allows the response of the material at a given point to depend on the collective deformation of all the bonds connected to that point. In other words, the force in a bond could depend on the net volume changes at the endpoints. The effect of this volume change, relative to the effect of the bond stretch, determines the Poisson's ratio and releases the limitation in the bond-based peridynamic applications. Since the equations of motion in peridynamics utilize integral form as opposed to the partial differential equations in the classical continuum mechanics, the enforcement of boundary conditions (Zhou and Du 2010) in peridynamics cannot follow the standard way as in the classical continuum theory and demands special treatments. Representative approaches of the special boundary condition treatments for peridynamics include the introduction of ghost particles (Parks *et al*. 2008), modification of the particle volume integration near the boundary (Kilic and Madenci 2010), and its combination with the finite element method (Oterkus *et al*. 2012).

Recently, a meshfree state-based peridynamic method (Bessa *et al.* 2013) was introduced to provide a link between the peridynamic and meshfree methods. It is concluded in their study that the discretization of state-based peridynamics leads directly to an approximation of the derivatives that can be obtained from the reproducing kernel particle method (RKPM) (Liu *et al*. 1995). Nevertheless, the conventional meshfree approximations such as the reproducing kernel (RK) approximation and the moving least-squared (MLS) approximation (Belytschko *et al*. 1994) do not verify the Kronecker-delta property on the boundary, thus further improvements for the enforcement of particle boundary conditions in the state-based peridynamics are needed. Convex kernel approximation (non-negative and exactly reproducing affine functions) (Wu and Koishi 2009, Wu *et al*. 2011) is a new meshfree approximation utilized to improve the boundary condition enforcement as well as solution accuracy in meshfree method. Convex kernel approximations possess the Kronecker-delta property on the boundary and avoid any special treatment on the essential boundaries. Park *et al.* (2011) embarked on a detailed dispersion analysis and reported that convex kernel approximation exhibits smaller lagging phase and amplitude errors than conventional non-convex approximation such as the RK and MLS approximations in full-discretization of the wave equation. Several meshfree and meshfree-enriched finite element Galerkin formulations (Wu and Hu 2011, Wu *et al.* 2012) using convex kernel approximations have been presented recently for the analyses of immersed composite (Wu *et al.* 2013), rubber-like materials in large deformation (Wu and Koishi 2012), and multi-scale acoustic waves (Wu and Hu 2013).

The aim of this paper is to introduce alternative boundary condition enforcement utilizing a convex kernel approximation for the state-based peridynamics that provides a stable and accurate solution for problems in solid mechanics applications. The reminder of the paper is outlined as follows: In the next section, we provide an overview on the state-based peridynamic formulation. In section 3, a spatial discretization for the state-based peridynamic formulation is described. In section 4, a localized convex kernel approximation is introduced and employed in the boundary

condition treatment for the state-based peridynamics. The conservation of linear momentum and angular momentum of the new formulation is also examined in the same section. Section 5 gives the final discrete equations for the peridynamic computation. Three numerical examples are presented in section 6 to illustrate the accuracy and robustness of the approach. Final remarks are drawn in section 7.

2. Overview on the state-based peridynamic formulation

Let's assume a body in the reference configuration occupies a region Ω_0. The state-based peridynamic equation of motion is given in the following equation (Silling *et al*.) as

$$\begin{aligned}\rho(\boldsymbol{X})\ddot{\boldsymbol{u}}(\boldsymbol{X},t) = \int_{\mathcal{H}_\delta} \left\{\underline{\boldsymbol{T}}[\boldsymbol{X},t]\langle \boldsymbol{X}'-\boldsymbol{X}\rangle - \underline{\boldsymbol{T}}[\boldsymbol{X}',t]\langle \boldsymbol{X}-\boldsymbol{X}'\rangle\right\} dV_{\boldsymbol{X}'} \\ + \boldsymbol{b}(\boldsymbol{X},t)\ \forall(\boldsymbol{X},t)\in\Omega_0\times(0,T)\end{aligned} \tag{1}$$

where $\boldsymbol{u(X,t)}$ is the displacement field. Eq. (1) is supplemented by initial conditions $\boldsymbol{u(X,0)}=\boldsymbol{u}_0\boldsymbol{(X)}$ and $\dot{\boldsymbol{u}}(\boldsymbol{X},0)=\dot{\boldsymbol{u}}_0(\boldsymbol{X})$. The vector $\boldsymbol{b(X,t)}$ is the body force density field and $\rho\boldsymbol{(X)}$ is the mass density. $\underline{\boldsymbol{T}}[\boldsymbol{X},t]$ is called the peridynamic force-vector state field. The angle brackets, $\langle\ \rangle$, in the integral indicate the vector on which the state field operates. In state-based peridynamics, $\underline{\boldsymbol{T}}[\boldsymbol{X},t]\langle \boldsymbol{X}'-\boldsymbol{X}\rangle : H_\delta \to \Re^3$ defines the force density vector of the material point $\boldsymbol{X}'$ exerting on the material point $\boldsymbol{X}$ within the "horizon region" H_δ. The "horizon region" $H_\delta \subset \Re^3$ describes the family of $\boldsymbol{X}'$ with respect to $\boldsymbol{X}$ and is defined by

$$H_\delta(\boldsymbol{X}) := \left\{(\boldsymbol{X}'-\boldsymbol{X})\in\Re^3 \,\middle|\, 0\le|\boldsymbol{X}'-\boldsymbol{X}|\le\delta\right\}\subset\Omega_0 \tag{2}$$

where δ is a radius of a open ball with center $\boldsymbol{X}\in\Re^3$ and $|\cdot|$ denotes the Euclidean vector or spectral matrix norm. If we define a vector valued function $\boldsymbol{f}$ by

$$\boldsymbol{f}(\boldsymbol{X}',\boldsymbol{X}) := \left\{\underline{\boldsymbol{T}}[\boldsymbol{X},t]\langle \boldsymbol{X}'-\boldsymbol{X}\rangle - \underline{\boldsymbol{T}}[\boldsymbol{X}',t]\langle \boldsymbol{X}-\boldsymbol{X}'\rangle\right\} \tag{3}$$

which represents the density of pairwise forces in the peridynamic bond that connects material points $\boldsymbol{X}$ and $\boldsymbol{X}'$, then we have the following anti-symmetric relationship for $\boldsymbol{f}$ that satisfies the Newton's third law.

$$\forall \boldsymbol{X}', \boldsymbol{X}\in\Re^3 : \boldsymbol{f}(\boldsymbol{X}',\boldsymbol{X}) = -\boldsymbol{f}(\boldsymbol{X},\boldsymbol{X}') \tag{4}$$

With this relationship, the peridynamic global balance of linear momentum is also assured (Silling *et al*. 2007).

In order to apply the conventional constitutive model in continuum mechanics to the state-based peridynamics, a deformation state $\underline{\boldsymbol{Y}}[\boldsymbol{X},t]$ is defined (Silling *et al*. 2007) in the following equation to map the peridynamic bonds connected to $\boldsymbol{X}$ into their images.

$$\underline{\boldsymbol{Y}}[\boldsymbol{X},t]\langle \boldsymbol{X}'-\boldsymbol{X}\rangle := \boldsymbol{x}(\boldsymbol{X}',t)-\boldsymbol{x}(\boldsymbol{X},t) \tag{5}$$

With Eq. (5), the relationship between the peridynamic force-vector state field $\underline{\boldsymbol{T}}[\boldsymbol{X},t]$ and the deformation state near material point $\boldsymbol{X}$ is described by $\underline{\boldsymbol{T}}[\boldsymbol{X},t]=\underline{\boldsymbol{T}}(\underline{\boldsymbol{Y}}[\boldsymbol{X},t])$. As given by Silling *et*

al. (2007), the nonlocal deformation gradient, $\overline{\boldsymbol{F}}$, at a material point $\boldsymbol{X}$ is expressed by

$$\overline{\boldsymbol{F}}(\boldsymbol{X},t)=\left[\int_{H_\delta}\omega(|\boldsymbol{X}'-\boldsymbol{X}|)(\underline{\boldsymbol{Y}}\langle\boldsymbol{X}'-\boldsymbol{X}\rangle\otimes(\boldsymbol{X}'-\boldsymbol{X}))dV_{X'}\right]\overline{\boldsymbol{K}}^{-1} \tag{6}$$

where $\omega(|\boldsymbol{X}'-\boldsymbol{X}|)$ is the influence function in H_δ and $\otimes$ denotes the dyadic product of two vectors. $\overline{\boldsymbol{K}}$ is a nonlocal shape tensor which is symmetric and given by

$$\overline{\boldsymbol{K}}=\int_{H_\delta}\omega(|\boldsymbol{X}'-\boldsymbol{X}|)((\boldsymbol{X}'-\boldsymbol{X})\otimes(\boldsymbol{X}'-\boldsymbol{X}))dV_{X'} \tag{7}$$

It is clear that the nonlocal shape tensor is positive definite if the influence function $\omega \geq 0$. The relation between the force vector $\underline{\boldsymbol{T}}[\boldsymbol{X},t]\langle\boldsymbol{X}'-\boldsymbol{X}\rangle$ and the nonlocal deformation gradient $\overline{\boldsymbol{F}}$ is conjugated through the following constitutive correspondence

$$\underline{\boldsymbol{T}}[\boldsymbol{X},t]\langle\boldsymbol{X}'-\boldsymbol{X}\rangle=\omega(|\boldsymbol{X}'-\boldsymbol{X}|)\overline{\boldsymbol{F}}\overline{\boldsymbol{S}}\overline{\boldsymbol{K}}^{-1}(\boldsymbol{X}'-\boldsymbol{X}) \tag{8}$$

where $\overline{\boldsymbol{S}}=\overline{\boldsymbol{S}}^T$ is the non-local second Piola-Kirchhoff stress tensor obtained from a classic constitutive law as a function of nonlocal deformation gradient $\overline{\boldsymbol{F}}$. Now the bond force between particles can be characterized in terms of strain and stress tensors, and thus allows for the use of the constitutive in peridynamic computation. This constitutive correspondence yields a state-based peridynamic formulation which satisfies the balance of angular momentum as proven in (Silling *et al*. 2007).

3. Spatial discretization

A direct integration based on particle value and a neglect of body force term lead to a discrete system of the state-based peridynamic equation of motion given by

$$\begin{aligned}\rho(\boldsymbol{X}_J)\ddot{\boldsymbol{u}}_J&=\sum_{I=1}^{NP}\left(\omega(|\boldsymbol{X}_I-\boldsymbol{X}_J|)\overline{\boldsymbol{F}}_J\overline{\boldsymbol{S}}_J\overline{\boldsymbol{K}}_J^{-1}(\boldsymbol{X}_I-\boldsymbol{X}_J)-\omega(|\boldsymbol{X}_J-\boldsymbol{X}_I|)\overline{\boldsymbol{F}}_I\overline{\boldsymbol{S}}_I\overline{\boldsymbol{K}}_I^{-1}(\boldsymbol{X}_J-\boldsymbol{X}_I)\right)V_I\\&=\sum_{I=1}^{NP}\left(\underline{\boldsymbol{T}}\langle\boldsymbol{X}_I-\boldsymbol{X}_J\rangle-\underline{\boldsymbol{T}}\langle\boldsymbol{X}_J-\boldsymbol{X}_I\rangle\right)V_I\\&=\sum_{I=1}^{NP}\boldsymbol{f}(\boldsymbol{X}_I,\boldsymbol{X}_J)V_I\end{aligned} \tag{9}$$

where the nonlocal deformation gradient $\overline{\boldsymbol{F}}$ and nonlocal shape tensor $\overline{\boldsymbol{K}}$ are also integrated using same trapezoidal rule to obtain

$$\overline{\boldsymbol{F}}_J=\sum_{I=1}^{NP}\left[V_I(\boldsymbol{X}_I)\omega(|\boldsymbol{X}_I-\boldsymbol{X}_J|)(\underline{\boldsymbol{Y}}\langle\boldsymbol{X}_I-\boldsymbol{X}_J\rangle\otimes(\boldsymbol{X}_I-\boldsymbol{X}_J))\right]\overline{\boldsymbol{K}}_J^{-1} \tag{10}$$

$$\overline{\boldsymbol{K}}_J=\sum_{I=1}^{NP}\left[V_I(\boldsymbol{X}_I)\omega(|\boldsymbol{X}_I-\boldsymbol{X}_J|)((\boldsymbol{X}_I-\boldsymbol{X}_J)\otimes(\boldsymbol{X}_I-\boldsymbol{X}_J))\right] \tag{11}$$

The nonlocal shape tensor $\overline{\boldsymbol{K}}$ acts like the moment matrix (Liu *et al*. 1995) in RKPM. In first-order RKPM, the approximation of displacement field is reproduced linearly. Similarly, the

approximation of deformation gradient in state-based peridynamics exactly reproduces the constant strain field. In discrete form, the nonlocal shape tensor of Eq. (11) remains symmetric and positive definite. In order to compare with the classical continuum mechanics theory, we rewrite the state-based peridynamic equation of motion in the following form

$$\begin{aligned} m_J \ddot{\boldsymbol{u}}_J &= \sum_{I=1}^{NP} \left(\omega\left(\left|\boldsymbol{X}_I - \boldsymbol{X}_J\right|\right) \overline{\boldsymbol{F}}_J \overline{\boldsymbol{S}}_J \overline{\boldsymbol{K}}_J^{-1} \left(\boldsymbol{X}_I - \boldsymbol{X}_J\right) - \omega\left(\left|\boldsymbol{X}_J - \boldsymbol{X}_I\right|\right) \overline{\boldsymbol{F}}_I \overline{\boldsymbol{S}}_I \overline{\boldsymbol{K}}_I^{-1} \left(\boldsymbol{X}_J - \boldsymbol{X}_I\right) \right) V_I V_J \\ &= \sum_{I=1}^{NP} \left(\overline{\boldsymbol{B}}_J^T \left(\boldsymbol{X}_I\right) \overline{\boldsymbol{F}}_J \overline{\boldsymbol{S}}_J V_J - \overline{\boldsymbol{B}}_I^T \left(\boldsymbol{X}_J\right) \overline{\boldsymbol{F}}_I \overline{\boldsymbol{S}}_I V_I \right) \end{aligned} \tag{12}$$

where $\overline{\boldsymbol{B}}$ matrix is the nonlocal displacement gradient matrix which is defined by

$$\overline{\boldsymbol{B}}_J \left(\boldsymbol{X}_I\right) = \begin{bmatrix} \overline{b}_{J,X} & 0 \\ 0 & \overline{b}_{J,Y} \\ \overline{b}_{J,Y} & \overline{b}_{J,X} \end{bmatrix} \tag{13}$$

with

$$\overline{b}_{J,X} \left(\boldsymbol{X}_I\right) = \frac{1}{\det\left(\overline{\boldsymbol{K}}\left(\boldsymbol{X}_J\right)\right)} \omega\left(\left|\boldsymbol{X}_I - \boldsymbol{X}_J\right|\right) \left(\left(X_I - X_J\right) \overline{K}_{22}\left(\boldsymbol{X}_J\right) - \left(Y_I - Y_J\right) \overline{K}_{12}\left(\boldsymbol{X}_J\right) \right) V_I \tag{14}$$

$$\overline{b}_{J,Y} \left(\boldsymbol{X}_I\right) = \frac{1}{\det\left(\overline{\boldsymbol{K}}\left(\boldsymbol{X}_J\right)\right)} \omega\left(\left|\boldsymbol{X}_I - \boldsymbol{X}_J\right|\right) \left(-\left(X_I - X_J\right) \overline{K}_{21}\left(\boldsymbol{X}_J\right) + \left(Y_I - Y_J\right) \overline{K}_{11}\left(\boldsymbol{X}_J\right) \right) V_I \tag{15}$$

It is noteworthy to mention that the $\overline{\boldsymbol{B}}$ matrix contains displacement gradients defined within the "horizon region" H_δ in an averaged sense. Different from the conventional displacement gradient matrix in Galerkin approach, the $\overline{\boldsymbol{B}}$ matrix in the state-based peridynamics contains no displacement derivatives.

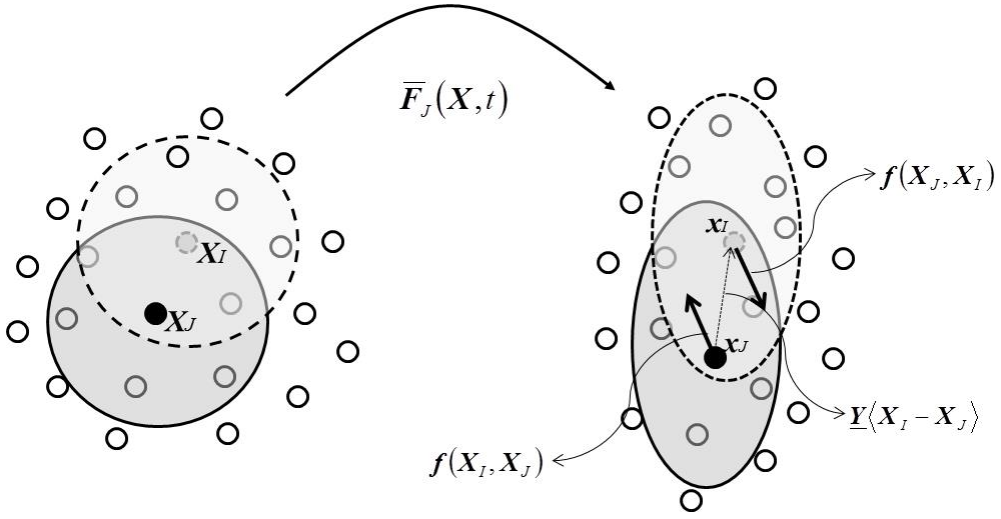

Fig. 1 Lagrangian mapping in peridynamics

This unique property allows the state-based peridynamic formulation to hold everywhere in Ω_0 whether or not displacement discontinuities are present. In comparison to the smoothed displacement gradients in the weak form of Galerkin meshfree method using stabilized conforming nodal integration method (SCNI) (Chen *et al*. 2000), the $\overline{\boldsymbol{B}}$ matrix in state-based peridynamics is evaluated point-wise in a strong form and does not meet the integration constraint (Chen *et al.* 2000) for the pass of constant stress patch test. It is also noted that the pairwise forces that connect material points $\boldsymbol{X}_I$ and $\boldsymbol{X}_J$ are opposite in direction but are not co-linear with their relative deformed position. Their magnitudes are not necessary equal, i.e., $\boldsymbol{f}(\boldsymbol{X}_I, \boldsymbol{X}_J)V_I \neq -\boldsymbol{f}(\boldsymbol{X}_J, \boldsymbol{X}_I)V_J$, unless the particle volumes are the same $V_I = V_J$ which is the case of regular particle distribution and the evaluated points are away from the boundary. The relation of pairwise forces is illustrated in Fig. 1.

4. Localization of particle boundary approximations

The enforcement of boundary conditions in peridynamics is non-trivial. This is because the particle force obtained from a function of pair-wise difference in displacement and coordinates is expressed in a nonlocal manner as defined in Eq. (1). As a consequence, the boundary conditions also cannot be imposed directly. The numerical issue of particle boundary condition enforcement in peridynamics can be illustrated by considering the following one-dimensional case as shown in Fig. 2. The one-dimensional rod has a length L and is under a regular discretization with an equally-spaced particle distance ΔX. The Young's modulus of the rod is denoted by E. We assume the cross-sectional area A of the rod is one. We further assume that the rod is fixed at one end and is subjected to a small displacement d at the other end. The discrete form of the state-based peridynamic equation of motion in Eq. (12) for this one-dimensional problem can be approximated by

$$\begin{aligned} \rho(X_J)\ddot{u}_J &= \sum_{I=I}^{NP}\left(\overline{B}_J(X_I)\overline{F}_J\overline{S}_J - \overline{B}_I(X_J)\overline{F}_I\overline{S}_I V_I/V_J\right) \\ &= f_J^1 - f_J^2 = f_J \end{aligned} \tag{16}$$

In Eq. (16), the nonlocal particle force density f_J for particle J consists of two parts. The first part is denoted by $f_J^1 = \overline{F}_J\overline{S}_J\sum_I^{NP}\overline{B}_J(X_I)$ in which $\overline{B}_J(X_I), I = 1\ldots NP$ resembles the concept of nonlocal gradient matrix (Chen *et al*. 2000) in Galerkin meshfree method for the analysis of strain localization problems. From this point of view, we can consider the state-based peridynamics is one kind of nonlocal methods for the regularization of strain localization problems. The second part of particle force density $f_J^2 = \sum_{I=1}^{NP}\overline{B}_I(X_J)\overline{F}_I\overline{S}_I V_I/V_J$ is a consistency term which is introduced to preserve the linear and angular momentum in multi-dimensional case. In the equivalent state, the analytical solution for the boundary particle force at X_1 is $\bar{f}_1 = f_1 \cdot V_1 = A \cdot d \cdot E/L = c$. We also assume the radius of influence function to be $\delta = 3\Delta X$ as used in most peridynamic examples. Using the fact that $\omega(|X_I - X_J|) = \omega(|X_J - X_I|)$, a simple but tedious calculation can show that the discrete peridynamic equation for the boundary particle X_I becomes

$$\begin{aligned}\bar{f}_1 &= \sum_{K=1}^{NP}\left(\overline{B}_1\left(X_K\right)\overline{F}_1\overline{S}_1V_1 - \overline{B}_K\left(X_1\right)\overline{F}_K\overline{S}_KV_K\right)\\ &= c\sum_{K=1}^{NP}\left(\overline{B}_1\left(X_K\right)V_1 - \overline{B}_K\left(X_I\right)V_K\right)\\ &= c\left\{\left(\frac{V_2}{\overline{K}_1}\right)\left(\omega\left(\left|X_2-X_1\right|\right)\left(X_2-X_1\right)V_1\right)+\left(\frac{V_3}{\overline{K}_1}\right)\left(\omega\left(\left|X_3-X_1\right|\right)\left(X_3-X_1\right)V_1\right)\right.\\ &\quad\left.-\left(\frac{V_1}{\overline{K}_2}\right)\left(\omega\left(\left|X_1-X_2\right|\right)\left(X_1-X_2\right)V_2\right)-\left(\frac{V_1}{\overline{K}_3}\right)\left(\omega\left(\left|X_1-X_3\right|\right)\left(X_1-X_3\right)V_3\right)\right\}\\ &\neq c\end{aligned} \tag{17}$$

where

$$\overline{K}_J = \sum_{I=1}^{NP}\left[V_I\left(X_I\right)\omega\left(\left|X_I - X_J\right|\right)\left(X_I - X_J\right)^2\right] \tag{18}$$

The result in Eq. (17) implies the boundary particle force computed by the standard state-based peridynamics does not reproduce the correct value. Apparently, the computed boundary particle force is numerically affected by the size and type of influence function.

For this reason, special numerical treatments (Parks *et al*. 2008, Kilic and Madenci 2010, Oterkus *et al*. 2012) are needed in the state-based peridynamics for the boundary condition enforcements. In this study, an alternative approach that considers a localized boundary particle approximation is developed to enforce the boundary conditions for the state-based peridynamics. This is achieved by introducing a meshfree convex approximation that restores the Kronecker-delta property at the boundary particles, leading to a localization of the influence function near the boundary and resulting in the direct boundary condition enforcement. In this study, we employ the GMF (Wu and Hu 2011) method to obtain the convex kernel approximation. Giving a convex hull $Convex(Z_I)$ of a particle set $Z_I = \{\boldsymbol{X}_I, I = 1,\cdots NP\} \subset \Re^3$ defined by

$$Convex\left(Z_I\right) = \left\{\sum_{I=1}^{NP}\alpha_I V_I \boldsymbol{X}_I \;\middle|\; \alpha_I \in \Re, \sum_{I=1}^{NP}\alpha_I V_I = 1, \alpha_I \geq 0, \boldsymbol{X}_I \in Z_I \right\} \tag{19}$$

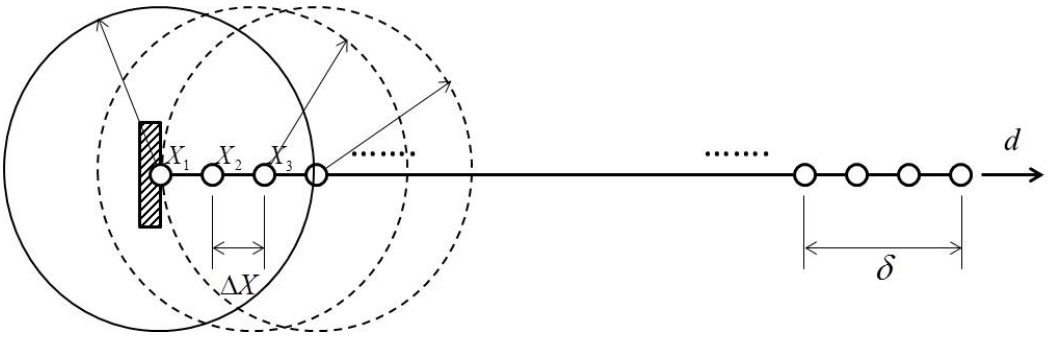

Fig. 2 One-dimensional linear bar under a uniform discretization and tension state

the GMF method is introduced to construct a convex approximation of a given (smooth) function ***x(X)*** such that the influence function $\omega_I : Convex(Z_I) \to \Re$ satisfies the following linear polynomial reproduction property

$$\sum_{I=1}^{NP} \widetilde{\omega}_I(\boldsymbol{X})\boldsymbol{X}_I = \boldsymbol{X} \;\; \forall \, \boldsymbol{X} \in Convex(Z_I) \tag{20}$$

where $\widetilde{\omega}_I(\boldsymbol{X})$ denotes a modified influence function for particle *I*. The first-order convex kernel approximation is constructed using the inverse tangent basis function, and the cubic spline window function is chosen to be the weight function in GMF method. Fig. 3 shows the two-dimensional modified influence function of an internal particle where its value is zero on the boundary. More detailed information about the derivation of GMF method and the corresponding mathematical properties can be found in (Wu *et al*. 2011).

With the introduction of new influence function, the modified gradient matrix evaluated at the boundary particle in one-dimension can be obtained by

$$\begin{aligned} \overline{B}_K(X_1) &= \frac{1}{\widetilde{K}_K}\widetilde{\omega}\left(|X_1 - X_K|\right)(X_1 - X_K)V_1 \\ &= \begin{cases} \dfrac{1}{\widetilde{K}_K}\widetilde{\omega}\left(|X_1 - X_K|\right)\underbrace{(X_1 - X_K)}_{=0}V_1 = 0, \;\; K = 1 \\ \dfrac{1}{\widetilde{K}_K}\underbrace{\widetilde{\omega}\left(|X_1 - X_K|\right)}_{=0}(X_1 - X_K)V_1 = 0, \; \forall \; K = 2, \cdots, NP \end{cases} \\ &= 0, \forall K = 1, \cdots, NP, X_1 \in \partial\Omega_0 \end{aligned} \tag{21}$$

where

$$\widetilde{K}_K = \sum_{I=1}^{NP}\left[\widetilde{\omega}\left(|X_I - X_K|\right)(X_I - X_K)^2 V_I\right] \neq 0, \forall \widetilde{\omega} \geq 0 \tag{22}$$

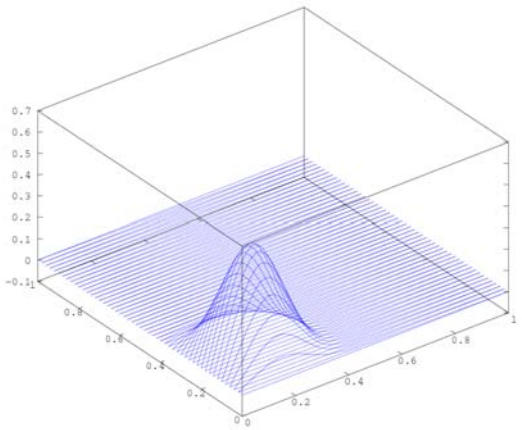

Fig. 3 A two-dimensional modified influence function of an internal particle decays to zero on the boundary

Note the non-negative property of the modified influence function $\widetilde{\omega} \geq 0$ and thus the invertibility of $\widetilde{K}$ is only verified in the convex kernel approximation and is not guaranteed in the conventional first-order RK or MLS approximations. Subsequently, one has

$$\bar{f}_1^2 = \sum_{K=1}^{NP} \left(\overline{B}_K (X_1) \overline{F}_K \overline{S}_K \right) V_K = 0, X_1 \in \partial\Omega_0 \tag{23}$$

Using the result in Eq. (23), the boundary particle force for X_1 can be now expressed by

$$\begin{aligned} \bar{f}_1 &= \sum_{K=1}^{NP} \left(\overline{B}_1 (X_K) \overline{F}_1 \overline{S}_1 V_1 - \overline{B}_K (X_1) \overline{F}_K \overline{S}_K V_K \right) \\ &= c \sum_{K=1}^{NP} \left(\overline{B}_1 (X_K) \right) V_1 \\ &= c \sum_{K=1}^{NP} \left(\frac{\widetilde{\omega}(X_K - X_1)(X_K - X_1) V_K V_1}{\sum_{J=1}^{NP} \widetilde{\omega}(X_J - X_1)(X_J - X_1)^2 V_J} \right) \\ &= c \frac{\sum_{K=1}^{NP} \left(\widetilde{\omega}(X_K - X_1)(X_K - X_1) V_K V_1 \right)}{\sum_{K=1}^{NP} \left(\widetilde{\omega}(X_K - X_1)(X_K - X_1)^2 V_K \right)} \end{aligned} \tag{24}$$

In general, we have $\widetilde{\omega}(X_K - X_1) \neq \widetilde{\omega}(X_1 - X_K)$ due to the convex approximation property. If we further assume that the modified influence function of boundary particle X_1 only covers to the neighbor particle X_2, then Eq. (24) becomes

$$\begin{aligned} \bar{f}_1 &= c \frac{\sum_{K=1}^{NP} \left(\widetilde{\omega}(X_K - X_1)(X_K - X_1) V_K V_1 \right)}{\sum_{K=1}^{NP} \left(\widetilde{\omega}(X_K - X_1)(X_K - X_1)^2 V_K \right)} \\ &= c \frac{\widetilde{\omega}(X_2 - X_1)(X_2 - X_1) V_2 V_1}{\widetilde{\omega}(X_2 - X_1)(X_2 - X_1)^2 V_2} \\ &= c \frac{\widetilde{\omega}(X_2 - X_1)(X_2 - X_1)^2}{\widetilde{\omega}(X_2 - X_1)(X_2 - X_1)^2} \\ &= c \end{aligned} \tag{25}$$

which recovers the correct boundary particle force. In other words, the convex kernel approximation is further localized near the boundary particle X_1 by resizing its influence function. With the localized convex kernel approximation, the enforcement of essential boundary condition and the prescribed particle force can be now directly applied to the peridynamic formulation in a standard way.

By localizing the particle boundary approximations in the standard nonlocal state-based peridynamics, it can be shown in the following that the discrete system remains to preserve the linear momentum in the multi-dimensional case.

$$\begin{aligned}
\int_{\Omega_0}\int_{\mathcal{H}_\delta} \boldsymbol{f}(\boldsymbol{X}_I,\boldsymbol{X}_J)dV_X dV_{X'} &\approx \sum_J \sum_I \boldsymbol{f}(\boldsymbol{X}_I,\boldsymbol{X}_J)V_I V_J \\
&= \sum_J \sum_I \left(\underline{\boldsymbol{T}}\langle \boldsymbol{X}_I - \boldsymbol{X}_J\rangle - \underline{\boldsymbol{T}}\langle \boldsymbol{X}_J - \boldsymbol{X}_I\rangle\right)V_I V_J \\
&= \sum_J \sum_I \underline{\boldsymbol{T}}\langle \boldsymbol{X}_I - \boldsymbol{X}_J\rangle V_I V_J - \sum_J \sum_I \underline{\boldsymbol{T}}\langle \boldsymbol{X}_J - \boldsymbol{X}_I\rangle V_I V_J \\
&= \sum_J \sum_I \underline{\boldsymbol{T}}\langle \boldsymbol{X}_I - \boldsymbol{X}_J\rangle V_I V_J - \sum_I \sum_J \underline{\boldsymbol{T}}\langle \boldsymbol{X}_I - \boldsymbol{X}_J\rangle V_J V_I \\
&= \boldsymbol{0}
\end{aligned} \tag{26}$$

Using the fact $\int_{\mathcal{H}_\delta} (\boldsymbol{x}' - \boldsymbol{x}) \otimes \underline{\boldsymbol{T}}\langle \boldsymbol{X}' - \boldsymbol{X}\rangle dV_{X'} \approx \sum_I (\boldsymbol{x}_I - \boldsymbol{x}_J) \otimes \underline{\boldsymbol{T}}\langle \boldsymbol{X}_I - \boldsymbol{X}_J\rangle V_I = 0$ (Silling *et al*. 2007), we proceed to show that the discrete system also satisfies the conservation of angular momentum.

$$\begin{aligned}
\int_{\Omega_0} \boldsymbol{x} \times \left(\int_{\mathcal{H}_\delta} (\boldsymbol{f}(\boldsymbol{X}', \boldsymbol{X}))dV_{X'}\right) dV_X &\approx \sum_J \boldsymbol{x}_J \times \sum_I \boldsymbol{f}(\boldsymbol{X}_I,\boldsymbol{X}_J)V_I V_J \\
&= \sum_J \boldsymbol{x}_J \times \sum_I \left(\underline{\boldsymbol{T}}\langle \boldsymbol{X}_I - \boldsymbol{X}_J\rangle - \underline{\boldsymbol{T}}\langle \boldsymbol{X}_J - \boldsymbol{X}_I\rangle\right)V_I V_J \\
&= \sum_J \sum_I \boldsymbol{x}_J \times \underline{\boldsymbol{T}}\langle \boldsymbol{X}_I - \boldsymbol{X}_J\rangle V_I V_J - \sum_J \sum_I \boldsymbol{x}_J \times \underline{\boldsymbol{T}}\langle \boldsymbol{X}_J - \boldsymbol{X}_I\rangle V_I V_J \\
&= \sum_J \sum_I \boldsymbol{x}_J \times \underline{\boldsymbol{T}}\langle \boldsymbol{X}_I - \boldsymbol{X}_J\rangle V_I V_J - \sum_I \sum_J \boldsymbol{x}_I \times \underline{\boldsymbol{T}}\langle \boldsymbol{X}_I - \boldsymbol{X}_J\rangle V_J V_I \\
&= -\sum_J \sum_I (\boldsymbol{x}_I - \boldsymbol{x}_J) \times \underline{\boldsymbol{T}}\langle \boldsymbol{X}_I - \boldsymbol{X}_J\rangle V_I V_J \\
&= \boldsymbol{0}
\end{aligned} \tag{27}$$

The results in Eqs. (26) and (27) hold for any choice of radius δ of the modified influence function $\widetilde{\omega}$ for interior particles and remain valid in irregular particle distribution.

5. Final discrete equations

When constitutive equations based on the rate form are used in multi-dimensional case, the nonlocal strain rate is calculated via the nonlocal velocity gradient. The nonlocal strain rate can be divided into a symmetric and an anti-symmetric part by

$$\dot{\bar{\boldsymbol{\varepsilon}}} = \frac{1}{2}\left(\overline{\nabla} \otimes \dot{\boldsymbol{x}} + \dot{\boldsymbol{x}} \otimes \overline{\nabla}\right) \tag{28}$$

$$\dot{\bar{\boldsymbol{W}}} = \frac{1}{2}\left(\overline{\nabla} \otimes \dot{\boldsymbol{x}} - \dot{\boldsymbol{x}} \otimes \overline{\nabla}\right) \tag{29}$$

where $\overline{\nabla}$ denotes the nonlocal gradient operator. The nonlocal gradient operator can be defined by

a nonlocal velocity gradient in the following discrete form given by

$$\overline{\nabla} \otimes \dot{\boldsymbol{x}}_J = \sum_{I=1}^{NP} \left[\overline{\omega}\left(\left| \boldsymbol{X}_I - \boldsymbol{X}_J \right| \right) \left(\underline{\dot{\boldsymbol{Y}}} \left\langle \boldsymbol{X}_I - \boldsymbol{X}_J \right\rangle \otimes \left(\boldsymbol{X}_I - \boldsymbol{X}_J \right) \right) V_I \right] \overline{\boldsymbol{K}}_J^{-1} \overline{\boldsymbol{F}}_J^{-1} \tag{30}$$

where the nonlocal deformation gradient $\overline{\boldsymbol{F}}$ and nonlocal shape tensor $\overline{\boldsymbol{K}}$ are computed by

$$\overline{\boldsymbol{F}}_J = \sum_{I=1}^{NP} \left[\widetilde{\omega}\left(\left| \boldsymbol{X}_I - \boldsymbol{X}_J \right| \right) \left(\underline{\boldsymbol{Y}} \left\langle \boldsymbol{X}_I - \boldsymbol{X}_J \right\rangle \otimes \left(\boldsymbol{X}_I - \boldsymbol{X}_J \right) \right) V_I \right] \overline{\boldsymbol{K}}_J^{-1} \tag{31}$$

$$\overline{\boldsymbol{K}}_J = \sum_{I=1}^{NP} \left[\widetilde{\omega}\left(\left| \boldsymbol{X}_I - \boldsymbol{X}_J \right| \right) \left(\left(\boldsymbol{X}_I - \boldsymbol{X}_J \right) \otimes \left(\boldsymbol{X}_I - \boldsymbol{X}_J \right) \right) V_I \right] \tag{32}$$

When the frame-indifferent Jaumann stress-rate is utilized in the formulation of the rate constitutive laws, the non-local Cauchy stress is updated by

$$\overline{\boldsymbol{\sigma}}^{n+1} = \overline{\boldsymbol{\sigma}}^{n} + \Delta \overline{\boldsymbol{\sigma}}^{n+1} + \left(\overline{\boldsymbol{\sigma}}^{n} \cdot \dot{\overline{\boldsymbol{W}}}^{n+1/2} - \dot{\overline{\boldsymbol{W}}}^{n+1/2} \cdot \overline{\boldsymbol{\sigma}}^{n} \right) \Delta t_n \tag{33}$$

It is also suffices to integrate the semi-discrete Eq. (9) by the central difference integration algorithm. The solution to Eq. (9) at *n-th* time step can be expressed by

$$m_J \ddot{\boldsymbol{u}}_J^n = \sum_{I=1}^{NP} \left(\overline{\boldsymbol{B}}_J^T \left(\boldsymbol{X}_I \right) \overline{\boldsymbol{F}}_J^n \overline{\boldsymbol{S}}_J^n V_J - \overline{\boldsymbol{B}}_I^T \left(\boldsymbol{X}_J \right) \overline{\boldsymbol{F}}_I^n \overline{\boldsymbol{S}}_I^n V_I \right) \tag{34}$$

Once the particle accelerations are solved, the particle velocities and displacements are updated by

$$\dot{\boldsymbol{U}}^{n+1/2} = \dot{\boldsymbol{U}}^{n-1/2} + \frac{\Delta t_{n+1} + \Delta t_n}{2} \ddot{\boldsymbol{U}}^n \tag{35}$$

$$\dot{\boldsymbol{U}}^{n+1} = \boldsymbol{U}^n + \Delta t_{n+1} \ddot{\boldsymbol{U}}^{n+1/2} \tag{36}$$

$$\boldsymbol{U}^{n+1} = \boldsymbol{U}^n + \Delta t_{n+1} \dot{\boldsymbol{U}}^{n+1/2} \tag{37}$$

The vector $\boldsymbol{U} = \left[\boldsymbol{u}_1, \ \boldsymbol{u}_2, \ \cdots \ , \boldsymbol{u}_{NP} \right]$ contains the particle displacements and $\dot{\boldsymbol{U}}$ denotes the corresponding particle velocities. The non-local second Piola-Kirchhoff stress tensor and non-local Cauchy stress tensor can be related by the standard push-forward and pull-back operations. The numerical stability of the explicit method is guided by a critical time step which can be approximated by the transit time of a dilatational wave over the shortest length scale in the system (Park *et al.* 2011). For the non-damped system of equations, the following time increment (Silling and Askari 2005) is adopted in the peridynamic computation

$$\Delta t = c_f \min_{I \in Z_I} \sqrt{\frac{2\rho_I}{\sum_J \frac{\bar{c}_I}{\left| \boldsymbol{x}_I - \boldsymbol{x}_J \right|} V_J}} \tag{38}$$

The value of $\bar{c}_I$ for particle *I* is taken to be $\bar{c}_I = \frac{18K}{\pi \delta_I^{\,4}}$ (Oterkus *et al.* 2012) where δ_I is the radius of influence function for particle *I*, and *K* is the material bulk modulus. The numerical

parameter c_f in Eq. (38) is a safety factor taken to be *0.5* in this paper.

6. Numerical examples

In this section, three benchmark examples are analyzed to study the performance of the present boundary condition treatment for the state-based peridynamic method. A Gaussian function (Tupek *et al*. 2013) is adopted to define the influence function ω in the standard state-based peridynamic method. No special boundary condition treatments are considered in the standard state-based peridynamic method. For the present method, the modified influence functions are constructed using the inverse tangent basis function, and the cubic spline window function is chosen to be the weight function in GMF method (Wu *et al*. 2011). The normalized radius of δ for the influence function is taken to be 3.0 which is the value normally used in the peridynamic computations for the macroscopic modeling. Finite element solution is also considered for the comparison. Dimensionless unit system is adopted in this paper for convenience.

6.1 1-D Bar subject to an End displacement

The one-dimensional bar in tension as shown in Fig. 4 is studied in this example. The bar has a length of 10.0 with cross-sectional area A = 1.0, density ρ = 0.01 and Young's modulus E = 100. The 1-D bar is discretized into 41 equally-spaced particles for the peridynamic method. Same 1-D bar is also discretized uniformly into 80 linear finite elements. The finite element solution will service as a reference solution in this example. The bar is under a displacement-control at a low speed of 0.0001 unit length per second to mimic the quasi-static state in a tension test.

The comparison results of particle displacements in 1-D bar are given in Fig. 5. As shown in Fig. 5, large displacement errors are observed in the standard state-based peridynamic solution without any special boundary condition treatments. The errors can be attributed to the low approximation order in the influence function and the inaccurate boundary condition enforcements in the standard peridynamic computation. On the other hand, the result of the present method shows good agreements with the reference solution generated by the FEM.

Fig. 6 compares the stress results with three different methods. As shown in Fig. 6, the standard state-based peridynamics not only produces severe error near the boundaries but also exhibits an amplitude error in the stress distribution. In comparison with standard peridynamic method, the present method improves the stress field and does not experience the amplitude error.

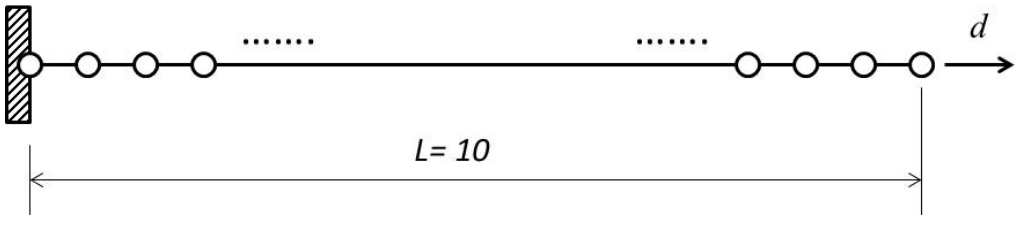

Fig. 4 A uniformly discretized 1-D bar subjected to displacement control in tension

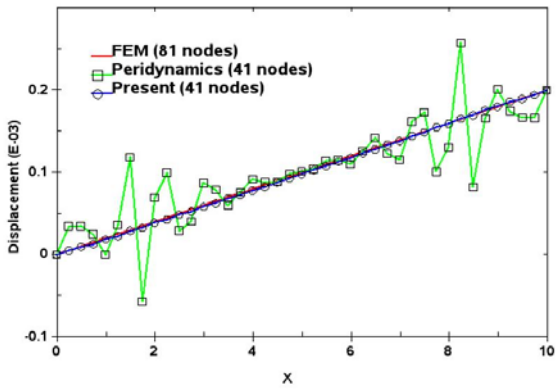

Fig. 5 The comparison of displacement fields in 1-D bar

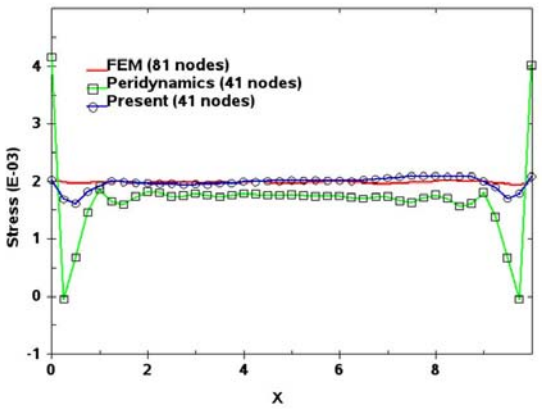

Fig. 6 The comparison of stress fields in 1-D bar

6.2. 1-D Bar subject to an Initial velocity

In this example, same 1-D bar in example 6.1 is considered and subjected to a uniform velocity of 1.0 as shown in the Fig. 7. In this wave propagation problem, the time-displacement responses are evaluated at the center of the bar for three comparison methods. As shown in Fig. 8, the standard state-based peridynamic method experiences the amplitude error as well as the phase error without accurate boundary condition enforcements. In particular, the phase error in displacement field increases as time advances. Similarly, the amplitude error and phase error are observed in the time-stress responses of the standard state-based peridynamic solution as depicted in Fig. 9. On other hand, the time-displacement solution of present method matches the FEM solution very well as demonstrated in Fig 8. The difference of time-stress response between the present method and FEM method is also marginal as shown in Fig. 9. The results in Figs. 8 and 9 indicate an improvement of accuracy in the state-based peridynamic solution using the proposed boundary condition treatment.

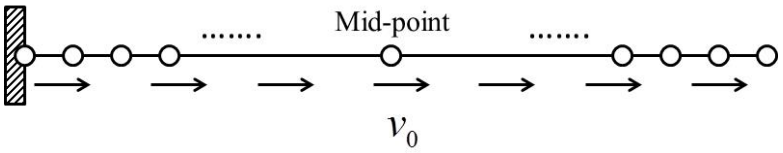

Fig. 7 A uniformly discretized 1-D bar subjected to initial velocity

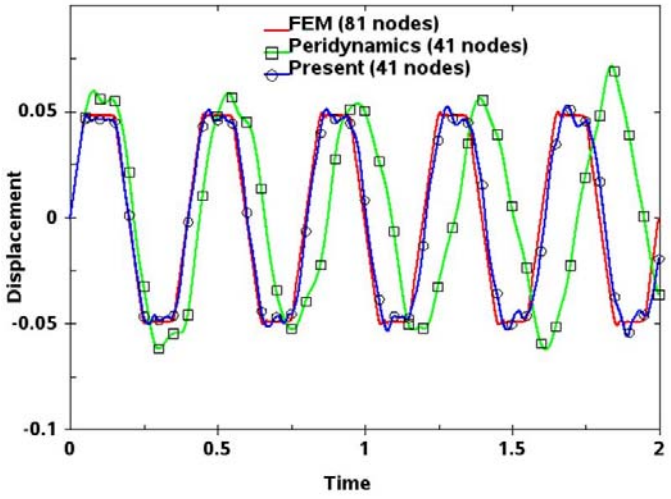

Fig. 8 The comparison of time-displacement responses in 1-D bar

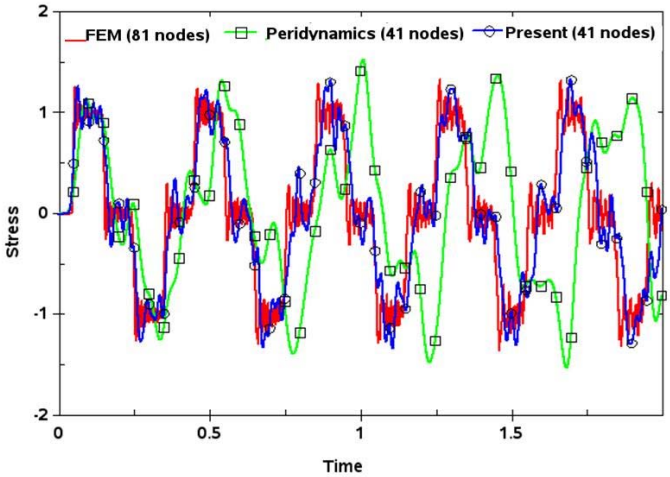

Fig. 9 The comparison of time-stress responses in 1-D bar

6.3 2-D compression test

A compression test of bounded elastic block is studied in this numerical example. The problem statement and boundary conditions of the example are given in Fig. 10. A discretization of 50 × 25 uniformly distributed nodes is used in the analysis. Same discretization is used for the finite element method based on bi-linear formulation. The material properties of the metal block are taken to be Young's modulus E = 100 and Poisson's ratio ν = 0.3. The density ρ = 100.0 is considered in this explicit dynamic analysis to have a larger time step. In this explicit dynamic analysis, the loading speed is taken to be very slow to mimic the quasi-static state. No artificial or bulk viscosity is considered in this analysis.

As shown in Fig. 11, the standard peridynamics experiences numerical instability and causes solution divergence in the early stage. The numerical instability is profound near the boundary and is apparently caused by the inappropriate boundary condition enforcement in the standard peridynamics. This numerical difficulty is similar to the one in 1-D problem and can be improved by the introduction of localized first-order convex kernel approximations. The deformation obtained by the present method is depicted in Fig. 12(b) which agrees well with the finite element solution as shown in Fig. 12(a). In Figs. 12(a) and 12(b), the contour plots are illustrated in terms of effective displacement fields. The comparison of σ_{yy} stress contours is given in Fig. 13. In Fig. 13, the stress field in the finite element solution is reported at the element center while the stress field of the present method is plotted particle-wise. As shown in Fig. 13, the present method generates a reasonable stress distribution which is comparable to one in the finite element method.

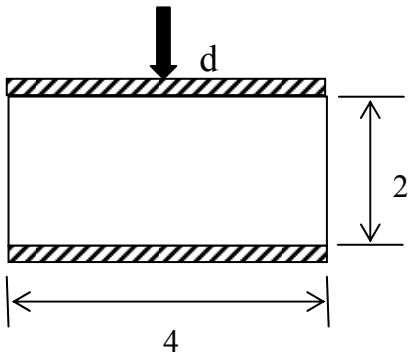

Fig. 10 The bounded elastic block model

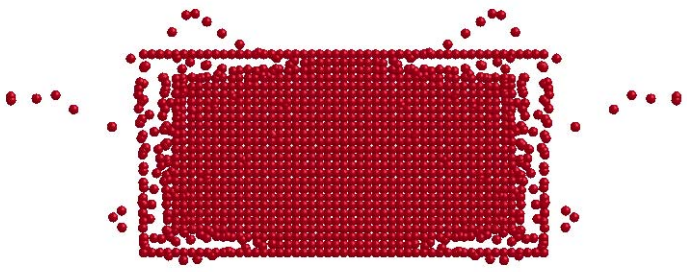

Fig. 11 Early divergence in the standard peridynamics

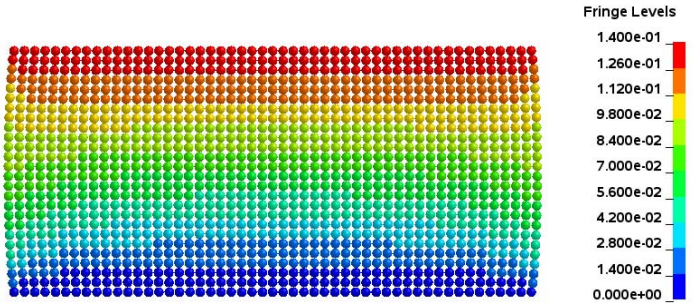

(a) FEM

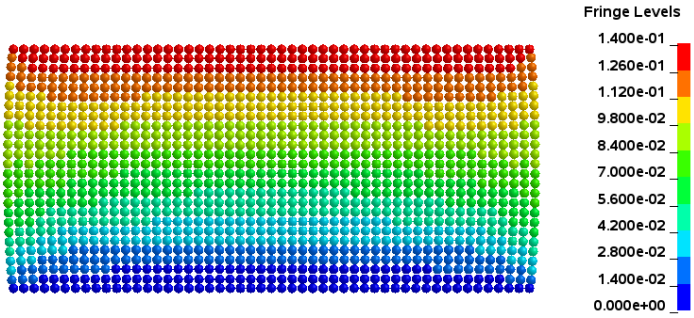

(b) Present method

Fig. 12 Comparison of effective displacement contour between the FEM and the present method

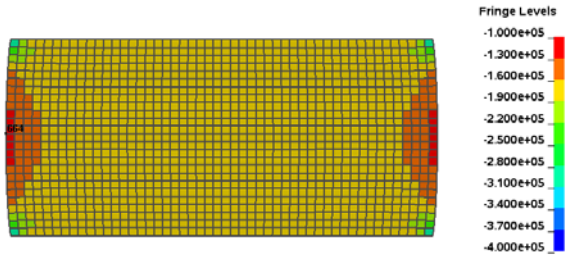

(a) FEM

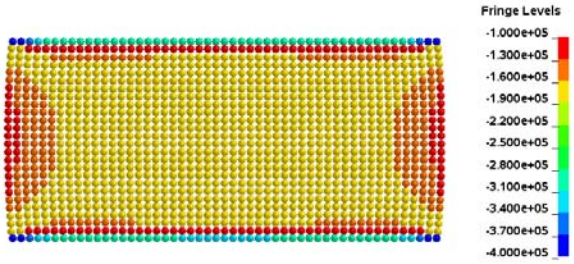

(b) Present method

Fig. 13 Comparison of σ_{yy} stress contour

7. Conclusions

A new approach for the enforcement of particle boundary conditions in the state-based peridynamic method is disclosed. This approach is based on a localization of particle boundary approximations in the nonlocal type of state-based peridynamic formulation to restore the Kronecker-delta property at the boundary particles. The localized convex kernel approximation is constructed by the GMF method and is shown to recover the correct boundary particle forces in a 1-D constant stress test. With the new particle boundary condition enforcements, the present approach is able to improve the solution accuracy of the standard state-based peridynamic method as demonstrated in the benchmark examples. In particular, remarkable improvements are made to the analysis of wave-propagation problem in which no major phase and amplitude errors are observed in the time-displacement as well as the time-stress responses of present solution. This nice feature is favored to provide an accurate peridynamic simulation in the material failure analysis using a stress-based failure criterion. The application of the new approach to the material failure analysis will be presented separately in a forthcoming paper. The development of a blending scheme to concurrently couple peridynamics and classical elasticity for multi-scale analysis will also be addressed in the near future.

Acknowledgements

The authors wish to thank Dr. John O. Hallquist of LSTC for his support to this research.

References

Askari, E., Bobaru, F., Lehoucq, R.B., Parks, M.L., Silling, S.A. and Weckner, O. (2008), "Peridynamics for multi-scale materials modeling", *J. Phys*. *Conference Series*, **125**, 012078.

Bazant, Z. and Jirasek, M. (2002), "Nonlocal integral formulations of plasticity and damage: survey and progress", *J. Eng. Mech. - ASCE*, **128**(11), 1119-1149.

Belytschko, T., Lu, Y.Y. and Gu, L. (1994), "Element-free Galerkin methods", *Int. J. Numer. Meth. Eng.*, **37**(2), 229-256.

Belytschko, T., Liu, W. K., Moran, B. and Elkhodary, K. (2014), Nonlinear *finite elements for continua and structures*, 2nd Ed., Wiley.

Bessa, M.A., Foster, J.T., Belytschko, T. and Liu, W. K. (2014), "A meshfree unification: reproducing kernel peridynamics", *Comput. Mech*., **53**(6), 1251-1264.

Chen, J.S., Wu, C.T. and Belytschko, T. (2000), "Regularization of material instabilities by meshfree approximations with intrinsic length scales", *Int. J. Numer. Meth. Eng*., **47**, 1303-1322.

Chen, J.S., Wu, C.T., Yoon, S. and You, Y. (2000), "A stabilized conforming nodal integration for Galerkin mesh-free methods", *Int. J. Numer. Meth. Eng.*, **50**, 435-466.

Chen, X. and Gunzburger, M. (2011), "Continuous and discontinuous finite element methods for a peridynamics model of mechanics", *Comput. Meth. Appl. Mech. Eng.*, **200**(9-12), 1237-1250.

Curtin, W.A. and Miller, R.E. (2003), "Atomistic/continuum coupling in computational materials science", *Model. Simul. Mater. Sc*., **11**, 33-68.

de Pablo, J.J. and Curtin, W.A. (2007), *Multi-scale modeling in advanced materials research: Challenges, novel methods, and emerging applications*, MRS Bulletin vol. 32, Material Research Society.

Kilic, B. and Madenci, E. (2010), "An adaptive dynamic relaxation method for quasi-static simulations using

the peridynamic theory", *Theor. Appl. Fract. Mec*., **53**(3), 194-204.
Liu, W.K., Jun, S. and Zhang, Y.F. (1995), "Reproducing kernel particle methods", *Int. J. Numer. Meth. Fl.*, **20**(8-9), 1081-1106.
McVeigh, C. and Liu, W. K. (2008), "Multi-resolution modeling of ductile reinforced brittle composites", *J. Mech. Phys. Solids*, **57** (2), 244-267.
Oterkus, E., Madenci, E., Weckner, O., Silling, S., Bogert, P. and Tessler, A. (2012), "Combined finite element and peridynamic analyses for predicting failure in a stiffened composite curved panel with a central slot", *Compos. Struct*., **94**(3), 839-850.
Parks, M.L., Lehoucq, R.B., Plimption, S. and Silling, S. (2008), "Implementing peridynamics withn a molecular dynamics code", *Comput. Phys. Commun*., **179**(11), 777-783.
Park, C.K., Wu, C.T. and Kan, C.D. (2011), "On the analysis of dispersion property and stable time step in meshfree method using the generalized meshfree approximation", *Finite Elem. Anal. Des.*, **47**(7), 683-697.
Ren, B. and Li, S.F. (2013), "A three-dimensional atomistic-based process zone model simulation of fragmentation in polycrystalline solids", *Int. J. Numer. Meth. Eng*., **93**(9), 989-1014.
Seleson, P., Parks, M.L., Gunzburger, M. and Lehoucq, R.B. (2010), "Peridynamics as an upscaling of molecular dynamics", *Multiscale Model. Sim*., **8**(1), 204-227.
Seleson, P. and Gunzburger, M. (2010), "Bridging methods for atomistic-to-continuum coupling and their implementation", *Commun. Comput. Phys*., **7**, 831-876.
Silling, S.A. (2000), "Reformulation of elasticity theory for discontinuities and long-range forces", *J. Mech. Phys. Solids*, **48**(1), 175-209.
Silling, S.A. and Askari, E. (2005), "A meshfree method based on the peridynamic model of solid mechanics", *Comput. Struct*., **83**(17-18), 1526-1535.
Silling, S.A., Epton, M., Weckner, O., Xu, J. and Askari, E. (2007), "Peridynamic states and constitutive modeling", *J. Elasticity*, **88**(2), 151-184.
Tupek, M.R., Rimoli, J.J. and Radovitzky, R. (2013), "An approach for incorporating classical continuum damage models in state-based peridynamics", *Comput. Meth. Appl. Mech. Eng.*, **263**, 20-26.
Watanabe, I. and Terada, K.A. (2010), "A method of predicting macroscopic yield strength of polycrystalline metals subjected to plastic forming by micro-macro de-coupling scheme", *Int. J. Mech. Sci*., **52(2)**, 343-355.
Wu, C.T. and Koish, M. (2009), "A meshfree procedure for the microscopic analysis of particle-reinforced rubber compounds", *Interact. Multiscale Mech*., **2**(2), 147-169.
Wu, C.T., Park, C.K. and Chen, J.S. (2011), "A generalized approximation for the meshfree analysis of solids", *Int. J. Numer. Meth. Eng*., **85**(6), 693-722.
Wu, C.T. and Hu, W. (2011), "Meshfree-enriched simplex elements with strain smoothing for the finite element analysis of compressible and nearly incompressible solids", *Comput. Meth. Appl. Mech. Eng*., **200**(45-46), 2991-3010.
Wu, C.T. and Koishi, M. (2012), "Three-dimensional meshfree-enriched finite element formulation for micromechanical hyperelastic modeling of particulate rubber composites", *Int. J. Numer. Meth. Eng.*, **91**(11), 1137-1157.
Wu, C.T., Hu, W. and Chen, J.S. (2012), "Meshfree-enriched finite element methods for the compressible and near-incompressible elasticity", *Int. J. Numer. Meth. Eng.*, **90**(7), 882-914.
Wu, C.T., Guo, Y. and Askari, E. (2013), "Numerical modeling of composite solids using an immersed meshfree Galerkin method", *Composit. B*, **45**(1), 1397-1413.
Wu, C.T. and Hu, W. (2013), "Multi-scale finite element analysis of acoustic waves using global residual-free meshfree enrichments, *Interact. Multiscale Mech*., **6**(2), 83-105.
Zhang, T. and Gunzburger, M. (2010), "Quadrature-rule type approximations to the quasi-continuum method for long-range interatomic interactions", *Comput. Meth. Appl. Mech. Eng.*, **199**(9-12), 648-659.
Zhou, K. and Du, Q. (2011), "Mathematical and numerical analysis of linear peridynamic models with nonlocal boundary conditions", *SIAM J. Numer. Anal*., **48(5)**, 1759-1780.